

## HIGH-DENSITY MOLECULAR GAS PROPERTIES OF THE STARBURST GALAXY NGC 1614 REVEALED WITH ALMA

MASATOSHI IMANISHI<sup>1,2</sup>

Subaru Telescope, 650 North A'ohoku Place, Hilo, Hawaii, 96720, U.S.A.

AND

KOUICHIRO NAKANISHI<sup>1,2</sup>

Joint ALMA Observatory, Alonso de Cordova 3107, Vitacura 763-0355, Santiago de Chile

AJ

## ABSTRACT

We present the results of HCN/HCO<sup>+</sup>/HNC J = 4–3 transition line observations of the nearby starburst galaxy NGC 1614, obtained with ALMA Cycle 0. We find that high density molecular gas, traced with these lines, shows a velocity structure such that the northern (southern) side of the nucleus is redshifted (blueshifted) with respect to the nuclear velocity of this galaxy. The redshifted and blueshifted emission peaks are offset by  $\sim 0.6''$  at the northern and southern sides of the nucleus, respectively. At these offset positions, observations at infrared  $> 3 \mu\text{m}$  indicate the presence of active dusty starbursts, supporting the picture that high-density molecular gas is the site of active starbursts. The enclosed dynamical mass within the central  $\sim 2''$  in radius, derived from the dynamics of the high-density molecular gas, is  $\sim 10^9 M_\odot$ , which is similar to previous estimates. Finally, the HCN emission is weaker than HCO<sup>+</sup> but stronger than HNC for J = 4–3 for all starburst regions of NGC 1614, as seen for J = 1–0 transition lines in starburst-dominated galaxies.

*Subject headings:* galaxies: active — galaxies: nuclei — galaxies: starburst — submillimeter: galaxies

## 1. INTRODUCTION

Luminous infrared galaxies (LIRGs) show strong infrared emission, with infrared (8–1000  $\mu\text{m}$ ) luminosities of  $L_{\text{IR}} > 10^{11} L_\odot$ , created by energy sources hidden behind dust. They are mostly found in gas-rich galaxy mergers (Sanders & Mirabel 1996). Molecular gas in galaxy mergers is largely influenced by merger-induced physical processes, and obtaining observational constraints on the spatial distribution and dynamics of molecular gas in merging LIRGs is important to our understanding of gas-rich galaxy merger processes. (Sub)millimeter interferometric observations of rotational J-transition lines of molecular gas are a powerful tool for this purpose. High-sensitivity, high-spatial-resolution ( $< a \text{ few arcsec}$ ) interferometric observations of merging LIRGs using bright CO molecular lines have been widely performed (Downes & Solomon 1998; Bryant & Scoville 1999; Trung et al. 2001; Evans et al. 2002; Downes & Eckart 2007). These CO observations at low-J transitions (J = 1–0 and 2–1) have effectively traced the low-density ( $10^{1-3} \text{ cm}^{-3}$ ) molecular gas properties in great detail due to the low dipole moment of CO ( $\mu \sim 0.1 \text{ debye}$ ). However, in merging LIRGs, the fraction of high density ( $> 10^4 \text{ cm}^{-3}$ ) molecular gas is much higher than in normal quiescent star-forming galaxies (Solomon et al. 1992; Gao & Solomon 2004), and it is within such high-density gas that stars are actually born. Thus, it is vital to obtain observational constraints of the properties of high-density molecular gas in merging LIRGs if we are to understand the essential physical processes in gas-rich

galaxy mergers.

Observations of molecular gas with high dipole moments, such as HCN, HCO<sup>+</sup>, and HNC ( $\mu > 3 \text{ debye}$ ), can effectively probe high-density molecular gas. However, these molecular lines are generally much fainter than the bright CO lines, and the spatial information of dense gas is still limited to nearby, very bright merging LIRGs only (Aalto et al. 1997; Casoli et al. 1999; Imanishi et al. 2004; Nakanishi et al. 2005; Imanishi et al. 2006b; Imanishi & Nakanishi 2006; Imanishi et al. 2007; Iono et al. 2007; Wilson et al. 2008; Imanishi et al. 2009; Aalto et al. 2009; Sakamoto et al. 2009, 2013). From these previously performed observations, it has been shown that the spatial distribution of high-density molecular gas is significantly different from that of low-density molecular gas, in that high-density gas is more concentrated in the nuclear regions of galaxies (Iono et al. 2004; Nakanishi et al. 2005; Imanishi et al. 2007; Wilson et al. 2008; Sakamoto et al. 2013). In merging LIRGs, it is in the nuclear regions where very violent processes, including starbursts (= active star-formation) and active mass accretion onto a supermassive black hole (SMBH) occur. Additionally, feedback to the surrounding interstellar medium and entire galaxy, if present, originates from these regions (Hopkins et al. 2005; Springel et al. 2005; Di Matteo et al. 2005; Hopkins et al. 2006). Spatially resolved interferometric observations using dense gas tracers are of particular importance in investigating the interesting nuclear regions of merging LIRGs.

Starburst and active galactic nucleus (AGN) activity powered by a mass-accreting SMBH can have different effects/feedback on the surrounding dense molecular gas at the merging LIRG's nuclei. It is proposed that starburst and AGN activity could be distinguishable based on the line flux ratios of dense molecular gas tracers (Kohn 2005; Imanishi et al. 2004, 2006b, 2007, 2009; Krips et

Electronic address: masa.imanishi@nao.ac.jp

<sup>1</sup> National Astronomical Observatory of Japan, 2-21-1 Osawa, Mitaka, Tokyo 181-8588

<sup>2</sup> Department of Astronomy, School of Science, Graduate University for Advanced Studies (SOKENDAI), Mitaka, Tokyo 181-8588

al. 2008) because (1) an AGN has an energy source with a much higher emission surface brightness than a starburst, and thus it can heat the surrounding dust and gas to higher temperature; and (2) an AGN emits stronger X-rays than a starburst does. Both of these factors could alter the chemical compositions of molecular gas in AGNs compared with starbursts (Meijerink & Spaans 2005; Lintott & Viti 2006; Harada et al. 2010); therefore, AGNs and starbursts could exhibit different molecular line flux ratios. High-spatial-resolution interferometric observations of multiple dense gas tracers can thus be used to scrutinize the processes deep inside the obscuring dust and gas in merging LIRG nuclei. With the advent of ALMA, such observations are now feasible.

NGC 1614 ( $z = 0.016$ ;  $L_{\text{IR}} = 10^{11.6} L_{\odot}$ ) is a well-studied, nearby LIRG. Merging signatures are clearly seen in the optical and near-infrared ( $1\text{--}2.5\ \mu\text{m}$ ) images as long, prominent tails around a single nucleus (Alonso-Herrero et al. 2001; Rothberg & Joseph 2004; Haan et al. 2011). It is classified as a starburst galaxy through optical spectroscopy (Veilleux et al. 1995; Kewley et al. 2001; Yuan et al. 2010). The infrared  $2.5\text{--}30\ \mu\text{m}$  spectrum of NGC 1614 is typical of a starburst-dominated galaxy with no AGN signature (Brandl et al. 2006; Bernard-Salas et al. 2009; Imanishi et al. 2010b; Vaisanen et al. 2012). The luminosities of the starburst-generated  $3.3\ \mu\text{m}$  polycyclic aromatic hydrocarbon (PAH) emission feature and the Br $\alpha$  ( $4.05\ \mu\text{m}$ ) hydrogen emission, measured through slitless spectroscopy and calculated relative to the total infrared ( $8\text{--}1000\ \mu\text{m}$ ) luminosity, are both as high as in starburst-dominated galaxies (Imanishi et al. 2010b), suggesting that the observed luminosity of NGC 1614 is totally accounted for by the detected starbursts, with no need for a significant AGN contribution. The infrared  $K$ -band ( $2.2\ \mu\text{m}$ ) spectrum shows a strong stellar-origin  $2.3\ \mu\text{m}$  CO absorption feature (Ridgway et al. 1994; Alonso-Herrero et al. 2001) and so supports the starburst-dominated scenario. High-spatial-resolution infrared  $8\text{--}20\ \mu\text{m}$  imaging observations reveal spatially extended, but compact ( $\sim 2''$ ), starburst-heated dust continuum emission (Miles et al. 1996; Soifer et al. 2001; Diaz-Santos et al. 2008; Imanishi et al. 2011), and the measured emission surface brightness is within the range explained by star formation, again requiring no significant contribution from an energetically important AGN (Soifer et al. 2001; Imanishi et al. 2011). The Pa $\alpha$  ( $1.88\ \mu\text{m}$ ) emission from star-forming HII-regions is dominated by nuclear  $\sim 3''$  area (Alonso-Herrero et al. 2001), which suggests that most of starburst activity in NGC 1614 is concentrated in the nuclear regions within  $< a\text{ few arcsec}$ .

Although ALMA is a very powerful tool for unveiling the molecular gas distribution in detail, it is not sensitive to spatially extended structure beyond the maximum scale, which is  $\sim 6''$  at  $\sim 350\ \text{GHz}$  in ALMA Cycle 0. The spatially resolved, but intrinsically compact ( $\sim 2''$ ) nuclear emission morphology and the known starburst-dominated nature make NGC 1614 an ideal target to investigate the spatial distribution and dynamics of dense molecular gas in merging LIRG nuclei, as well as to obtain a template of line flux ratios of dense gas tracers in starburst-dominated galaxies, during ALMA Cycle 0.

We thus performed ALMA band 7 ( $275\text{--}373\ \text{GHz}$ ) observations of NGC 1614 to study the emission properties

of HCN  $J = 4\text{--}3$ , HCO $^+$   $J = 4\text{--}3$ , and HNC  $J = 4\text{--}3$  lines. The basic information of NGC 1614 is summarized in Table 1. Throughout this paper, we adopt  $H_0 = 71\ \text{km s}^{-1}\ \text{Mpc}^{-1}$ ,  $\Omega_M = 0.27$ , and  $\Omega_\Lambda = 0.73$  (Komatsu et al. 2009), where  $1''$  corresponds to  $\sim 320\ \text{pc}$  at the distance of NGC 1614 ( $z = 0.016$ ).

## 2. OBSERVATIONS AND DATA ANALYSIS

All observations were made during ALMA Cycle 0 within the program 2011.0.00020.S (PI = M. Imanishi). Observation details are described in Table 2. We adopted the widest  $1.875\ \text{GHz}$  band mode, and the total channel number was 3840.

For NGC 1614 ( $z = 0.016$ ), HCN  $J = 4\text{--}3$  ( $\nu_{\text{rest}} = 354.505\ \text{GHz}$ ), and HCO $^+$   $J = 4\text{--}3$  ( $\nu_{\text{rest}} = 356.734\ \text{GHz}$ ) lines are simultaneously observable in ALMA band 7. Four frequency setups can cover four different frequencies at the same time. Two were used to observe HCN  $J = 4\text{--}3$  (central frequency was set as  $\nu_{\text{center}} = 348.922\ \text{GHz}$ ) and HCO $^+$   $J = 4\text{--}3$  lines ( $\nu_{\text{center}} = 350.920\ \text{GHz}$ ), and the remaining two were used to measure the continuum flux level ( $\nu_{\text{center}} = 337.106\ \text{GHz}$  and  $338.681\ \text{GHz}$ ). The net on-source exposure time for the HCN/HCO $^+$   $J = 4\text{--}3$  line observation of NGC 1614 was  $\sim 26\ \text{min}$ .

The frequency of the HNC  $J = 4\text{--}3$  line ( $\nu_{\text{rest}} = 362.630\ \text{GHz}$ ) is separated from the HCN  $J = 4\text{--}3$  and HCO $^+$   $J = 4\text{--}3$  lines, and we required independent observations. The HNC line was covered with one spectral window ( $\nu_{\text{center}} = 356.920\ \text{GHz}$ ), and an additional second spectral window was used to probe the continuum emission ( $\nu_{\text{center}} = 345.079\ \text{GHz}$ ). The net on-source exposure time for the HNC  $J = 4\text{--}3$  line observation of NGC 1614 was  $\sim 25\ \text{min}$ .

We started data analysis from calibrated data provided by the Joint ALMA Observatory. We first checked the visibility plots to see if the signatures of the emission lines were recognizable. The presence of HCN, HCO $^+$ , and HNC  $J = 4\text{--}3$  lines were evident in the visibility plot, whereas signatures of other molecular lines were not clearly seen. We then selected channels that were free from strong line emission to estimate the continuum flux level. We subtracted this continuum level and performed the task “clean” for molecular emission lines. The “clean” procedure was applied also to the continuum data. We employed 40-channel spectral binning ( $\sim 17\ \text{km s}^{-1}$ ) and  $0.3''\ \text{pixel}^{-1}$  spatial binning in this clean procedure.

## 3. RESULTS

Continuum emission properties are shown in Figure 1 and Table 3. Figure 2 displays the integrated intensity (moment 0) maps of molecular lines and spectra within the beam size at the continuum peak positions. Continuum emission is found to be well subtracted in the spectra (Figure 2 right panels), and so the moment 0 maps in Figure 2 (left) should reflect the properties of individual molecular gas emission lines. The peak flux, rms noise level, and synthesized beams in individual maps are summarized in Table 4 (row denoted “all”). The peak positions of HCN  $J = 4\text{--}3$  and HCO $^+$   $J = 4\text{--}3$  agree with that of continuum “a”, whereas that of HNC  $J = 4\text{--}3$  is two pixels ( $0.6''$ ) displaced to the south from the continuum “b” peak.

CS  $J = 7\text{--}6$  line at  $\nu_{\text{rest}} = 342.883\ \text{GHz}$  is covered in a

spectral window during the observations of HCN/HCO<sup>+</sup> J = 4–3 line, but it is not clearly detected in the spectrum (within the beam size) at the nucleus, which is defined from the continuum “a” emission peak (Figure 2, right). Because the signals of the CS J = 7–6 emission are not clearly seen, to create the moment 0 map of CS J = 7–6, we refer to the velocity profile of the brightest HCO<sup>+</sup> J = 4–3 emission line at the nucleus and sum signals with  $v_{\text{opt}} \equiv c (\lambda - \lambda_0) / \lambda_0 = 4600\text{--}4925$  [km s<sup>−1</sup>]. No clear CS J = 7–6 emission line is seen ( $< 3\sigma$ ) in the moment 0 map (Figure 2, left and Table 4). This undetected CS J = 7–6 line will not be used in the following discussion.

The moment 0 maps in Figure 2 display spatially extended structures compared with the beam size, particularly for HCN and HCO<sup>+</sup> J = 4–3 lines. We created spectra of the HCN, HCO<sup>+</sup>, and HNC J = 4–3 lines, integrated over all regions with significant signal detection ( $\sim 3'' \times 3''$ ), in Figure 3. All show double-peaked emission profiles, as seen in the <sup>12</sup>CO J = 2–1, <sup>12</sup>CO J = 3–2, and <sup>13</sup>CO J = 2–1 lines (Wilson et al. 2008). We applied double Gaussian fits. The derived parameters are summarized in Table 5 (rows denoted with “all”). For HCO<sup>+</sup> J = 4–3 emission, a triple Gaussian fit was also applied because three emission peaks were seen. The molecular line luminosities, integrated over regions of significant signal detection (corresponding to “all” in Table 5) are summarized in Table 6, where we adopted equations (2) and (3) of Solomon & Vanden Bout (2005).

Previously obtained high-spatial-resolution images of starburst indicators, such as the Pa $\alpha$  emission line (1.88  $\mu\text{m}$ ), the PAH emission feature (3.3  $\mu\text{m}$ ), the infrared 8.7  $\mu\text{m}$  continuum, and the radio 5–8.4 GHz (3.6–6 cm) continuum, have revealed the presence of ring-shaped circumnuclear starbursts with radii of 0.5–1.0'' (Neff et al. 1990; Alonso-Herrero et al. 2001; Diaz-Santos et al. 2008; Olsson et al. 2010; Vaisanen et al. 2012). A similar ring pattern is discernible in the high-spatial-resolution (0.5''  $\times$  0.4'') CO J = 2–1 molecular line map (Konig et al. 2013). Our ALMA map has a resolution of 1.5''  $\times$  1.3''. In this map, particularly in the brightest HCO<sup>+</sup> J = 4–3 line, where the highest S/N ratios are achieved, the emission is more elongated toward the north-south direction than the east-west direction, suggesting that a larger amount of high-density molecular gas is distributed at the northern and southern part of the nucleus.

Figure 4 displays the intensity weighted mean velocity (moment 1) and intensity weighted velocity dispersion (moment 2) maps of HCN and HCO<sup>+</sup> J = 4–3 lines. The dense molecular gas in the northern (southern) part of the nucleus is clearly redshifted (blueshifted) relative to the nuclear velocity of NGC 1614 ( $v_{\text{opt}} = 4800$  [km s<sup>−1</sup>] for  $z = 0.016$ ). The contours of emission of the red component with  $v_{\text{opt}} > 4800$  [km s<sup>−1</sup>] and the blue component with  $v_{\text{opt}} < 4800$  [km s<sup>−1</sup>] are displayed in Figure 5. The emission properties of the red and blue components are summarized in Table 4 (rows denoted with “red” and “blue”). The emission peak positions of the red and blue components are shifted by two pixels (0.6'') to the north and south direction, respectively, from the nucleus. For HNC J = 4–3 emission in Figure 5, the blue component is much brighter than the red component, which could explain the slight peak offset in the HNC J = 4–3 moment 0 map (integrated over all ve-

locity components with significant signal detection) with respect to the nuclear position (Table 3).

Spectra within the beam size, at the nuclear position and the peak position of the red and blue components, are shown in Figure 6. As expected, spectra at the red (blue) component peaks are redshifted (blueshifted), relative to those at the nuclear position for all the HCN, HCO<sup>+</sup>, and HNC J = 4–3 lines. Gaussian fits were applied to the spectra. The resulting parameters are shown in Table 5 (rows denoted with “peak”, “red”, and “blue”). The line widths of these dense molecular gas tracers are generally larger in the blue component than the red component, which has also been seen in ionized gas (De Robertis & Shaw 1988). This indicates that the southern part of the nucleus is more turbulent than the northern part.

Figure 7 presents the position-velocity diagram along the north-south direction, passing through the nucleus. The channel map of the brightest HCO<sup>+</sup> J = 4–3 emission line is shown in Figure 8. The dense molecular gas in the northern region has greater velocity (more redshifted) than the southern molecular gas.

#### 4. DISCUSSION

##### 4.1. Spatial distribution of dense molecular gas

The red and blue components of the dense molecular gas show emission peaks at  $\sim 0.6''$  north and south of the nucleus, respectively, roughly corresponding to the northern and southern parts of the previously identified circumnuclear starburst ring with a radius of 0.5–1'' (Neff et al. 1990; Alonso-Herrero et al. 2001; Diaz-Santos et al. 2008; Olsson et al. 2010; Vaisanen et al. 2012). Vaisanen et al. (2012) investigated the spatial distribution of the 3.3  $\mu\text{m}$  PAH emission feature, and found particularly strong PAH emission at the northern and southern parts of the ring. The 3.3  $\mu\text{m}$  PAH emission is a good indicator of starburst activity (Moorwood 1986; Imanishi & Dudley 2000; Imanishi et al. 2006a, 2008, 2010b).

In contrast, the Pa $\alpha$  (1.88  $\mu\text{m}$ ) emission, originating in HII regions, is strongest at the eastern and western sides of the circumnuclear starburst ring (Alonso-Herrero et al. 2001). How are these two kinds of starbursts related? One scenario involves an age difference. The eastern and western starburst regions are probed with the tracers of HII regions where plenty of ionizing ( $\lambda < 912$  Å) UV photons, usually dominated by short-lived massive O-stars, are needed. In contrast, the 3.3  $\mu\text{m}$  PAH emission mostly comes from photo-dissociation regions between HII regions and molecular gas, where PAHs are excited by non-ionizing ( $\lambda > 912$  Å) stellar UV photons (Sellgren 1981). For the PAH-exciting non-ionizing UV continuum, the contribution from less massive stars than O stars is higher than that for ionizing UV photons inside HII regions. Thus, the PAH emission feature is sensitive not only to very young O-stars dominant starbursts but also to slightly aged starbursts where massive O-stars have mostly died, but less massive stars (e.g., B-stars) still survive and emit a sufficient quantity of non-ionizing PAH-exciting UV photons. Diaz-Santos et al. (2008) showed that the 8.7  $\mu\text{m}$  infrared dust continuum, relative to the HII region tracer Pa $\alpha$  line (1.88  $\mu\text{m}$ ), is enhanced at the northern and southern starburst ring. Because non-ionizing UV continuum emission can contribute significantly to the infrared continuum emission but cannot

do so for the  $\text{Pa}\alpha$  emission, the observed spatial variation in the  $3.3\ \mu\text{m}$  PAH to  $\text{Pa}\alpha$  and  $8.7\ \mu\text{m}$  to  $\text{Pa}\alpha$  flux ratio is explainable under the scenario that the typical starburst age is older at the northern and southern ring than at the eastern and western ring (Diaz-Santos et al. 2008). If the circumnuclear starburst ring is formed by nuclear starbursts that are progressing outward (Alonso-Herrero et al. 2001), the age difference in starbursts at different positions of the ring needs to be explained.

Dust extinction is another possibility because  $\text{Pa}\alpha$  emission at  $1.88\ \mu\text{m}$  can be more highly flux-attenuated than the  $3.3\ \mu\text{m}$  PAH emission and the  $8.7\ \mu\text{m}$  dust continuum. Radio free-free continuum emission from HII regions is less susceptible to foreground dust extinction and could help to determine whether  $\text{Pa}\alpha$  emission is significantly affected by dust extinction. High-spatial-resolution radio continuum maps at 5 GHz (6 cm) and 8.4 GHz (3.6 cm) are available (Neff et al. 1990; Olsson et al. 2010) and Olsson et al. (2010) ascribe the radio 5 GHz and 8.4 GHz emission in NGC 1614 to free-free emission from HII-regions in young starbursts. Because the effects of free-free absorption inside HII regions are smaller at 8.4 GHz than at 5 GHz, the 8.4 GHz radio emission map is taken as the better probe of the true spatial distribution of HII regions.

In the radio 8.4 GHz map, strong emission is detected in the eastern and western starburst ring (Olsson et al. 2010; König et al. 2013), as seen in  $\text{Pa}\alpha$  line map (Alonso-Herrero et al. 2001), confirming that luminous HII regions are present at those locations. However, at 8.4 GHz, bright emission is seen also at the northern starburst ring, where  $\text{Pa}\alpha$  emission is not strong (König et al. 2013). Similarly, when compared with the eastern starburst ring, the southern starburst ring is more conspicuous at 8.4 GHz than in  $\text{Pa}\alpha$  (König et al. 2013). The comparison of the radio 8.4 GHz (3.6 cm) and  $1.88\ \mu\text{m}$   $\text{Pa}\alpha$  emission indicates that HII-regions at the northern and southern parts of the starburst ring, unveiled by the radio 8.4 GHz emission, are not sufficiently distinguished by  $\text{Pa}\alpha$  emission. These northern and southern regions of the starburst ring are the locations where dense molecular gas is distributed, according to our ALMA data. Given that dust coexists with dense molecular gas, dust extinction is a natural explanation for the small  $\text{Pa}\alpha$  to 8.4 GHz flux ratio at the northern and southern starburst rings. Weak dust extinction is reported for starburst regions in NGC 1614 compared with other general starburst galaxies (Alonso-Herrero et al. 2001), based on near-infrared observations at  $\lambda < 2\ \mu\text{m}$ . This could be due partly to the fact that observations at  $\lambda < 2\ \mu\text{m}$ , including  $\text{Pa}\alpha$  emission, selectively trace emission from less dusty starburst regions at the eastern and western ring and do not properly probe the dusty starbursts at the northern and southern parts of the ring due to flux attenuation by dust extinction.

#### 4.2. Dynamics of dense molecular gas

Our ALMA data show that the high-density molecular gas in the northern part of the nucleus is redshifted and that gas in the southern part is blueshifted with respect to the nuclear velocity of this galaxy. This suggests the rotation of dense molecular gas along the east-west axis (Neff et al. 1990). A similar velocity pattern was found previously in the ionized gas maps (De Robertis & Shaw

1988) and the lower density molecular gas probed with CO  $J = 3-2$  and  $J = 2-1$  (Wilson et al. 2008; König et al. 2013). The observed velocity dispersion is highest in the nuclear region with  $\sim 80\ \text{km s}^{-1}$  (Figure 4), although it may be affected by the beam smearing of a rotating motion at the center. This value is similar to those measured through near-infrared spectroscopy (Shier et al. 1994) and with (sub)millimeter CO  $J = 3-2$  and CO  $J = 2-1$  emission lines (Wilson et al. 2008).

The rotational motion found in our moment 1 maps (Figure 4) can be used to derive the dynamical mass inside the rotating dense molecular gas disk. We used the  $\text{HCO}^+$   $J = 4-3$  line because it is brighter than HCN  $J = 4-3$ , and so the achieved S/N ratios are higher. In Figure 4, the rotational velocity is  $v \sim 100\ \text{km s}^{-1}$  at  $1.5-2''$  (or  $r = 480-640\ \text{pc}$  at  $z = 0.016$ ) from the nucleus. The derived dynamical mass within  $1.5-2''$  radius is  $M_{\text{dyn}} = rv^2/G/\sin(i)^2 = 1.5-2.5 \times 10^9 M_{\odot}$ , where the inclination angle  $i = 51^\circ$  is adopted (De Robertis & Shaw 1988; Alonso-Herrero et al. 2001). This mass is comparable to the previously estimated values (Shier et al. 1994; Alonso-Herrero et al. 2001; Olsson et al. 2010).

#### 4.3. Flux ratios of dense gas tracers

Figure 9 is a plot of HCN-to- $\text{HCO}^+$  and HCN-to-HNC flux ratios at the  $J = 4-3$  transition, derived from the spectra at the nucleus, red component peak position, blue component peak, and all regions with significant signal detection. In all data, HCN  $J = 4-3$  flux is smaller than that of  $\text{HCO}^+$   $J = 4-3$ , but higher than HNC  $J = 4-3$  flux.

Using the  $J = 1-0$  transitions of HCN,  $\text{HCO}^+$ , and HNC, the possibility of distinguishing the hidden energy sources of merging LIRG's dusty nuclei is suggested (Kohno 2005; Imanishi et al. 2004, 2006b, 2007; Perez-Beaupuits et al. 2007; Krips et al. 2008; Imanishi et al. 2009; Costagliola et al. 2011). In general, HCN-to- $\text{HCO}^+$  flux ratios are small ( $< 1$ ), and HCN-to-HNC flux ratios are large ( $> 1$ ) in starburst-dominated galaxies, whereas HCN-to- $\text{HCO}^+$  flux ratios can be high ( $> 1$ ) in AGNs. AGNs could enhance HCN flux relative to  $\text{HCO}^+$ , due possibly to HCN abundance enhancement by AGN radiation (Harada et al. 2010) and/or infrared radiative pumping of HCN (Sakamoto et al. 2010). The low HCN-to- $\text{HCO}^+$  flux ratios obtained in the starburst-dominated galaxy NGC 1614 at  $J = 4-3$  are similar to other starburst galaxies at  $J = 1-0$ . To obtain a physical interpretation of the observed  $J = 4-3$  flux ratio, we need to know the excitation conditions.

The HCN  $J = 1-0$  flux of NGC 1614 was found to be  $7.2\ [\text{Jy km s}^{-1}]$  by Gao & Solomon (2004) based on single dish telescope observations. Under thermal excitation, the HCN  $J = 4-3$  flux is expected to be 16 times higher than  $J = 1-0$ , and so  $\sim 115\ [\text{Jy km s}^{-1}]$ . Our ALMA observations provide an observed HCN  $J = 4-3$  flux from all signal-detected regions of  $2.8\ [\text{Jy km s}^{-1}]$ . The smaller flux of our ALMA data could partly be caused by missing flux, as our ALMA observations are insensitive to spatially extended emission with  $> 6''$ . Scoville et al. (1989) and Wilson et al. (2008) estimated that in NGC 1614, the nuclear ( $< \text{several arcsec}$ ) CO  $J = 1-0$  and  $J = 3-2$  emission can account for  $> 30\%$  and  $> 45\%$  of the total flux measured with single-dish telescopes. Because the HCN  $J = 4-3$  line traces higher density molecular gas

( $>10^6 \text{ cm}^{-3}$ ) than do CO  $J = 1-0$  and  $J = 3-2$  lines and because higher-density gas is more concentrated in the nuclear region, our ALMA HCN  $J = 4-3$  data should recover  $>45\%$  of the total flux. Even assuming a missing flux of a factor of  $\sim 2$ , the HCN  $J = 4-3$  flux of NGC 1614 is  $5.6 \text{ [Jy km s}^{-1}\text{]}$ , only  $<5\%$  of the expected flux ( $115 \text{ Jy km s}^{-1}$ ) for thermal excitation. Thus, HCN  $J = 4-3$  line is significantly sub-thermally excited in NGC 1614, as observed in nearby galaxies at  $>100 \text{ pc}$  scale (Knudsen et al. 2007).

Since the critical density of HCN  $J = 4-3$  ( $n_{\text{crit}} \sim 2 \times 10^7 \text{ cm}^{-3}$ ) is higher than that of  $\text{HCO}^+ J = 4-3$  ( $n_{\text{crit}} \sim 4 \times 10^6 \text{ cm}^{-3}$ ) (Meijerink et al. 2007),  $\text{HCO}^+ J = 4-3$  is more easily excited than HCN  $J = 4-3$  in starbursts. In an AGN, the emission surface brightness is higher than starburst activity, so the surrounding dust and gas are heated to a higher temperature, which may help to excite HCN  $J = 4-3$  more than starburst activity. A high HCN-to- $\text{HCO}^+ J = 4-3$  flux ratio could be a good diagnostic of an AGN, simply because of the high excitation of HCN  $J = 4-3$  in an AGN, even without an HCN-abundance enhancement (Harada et al. 2010). HCN-to- $\text{HCO}^+$  flux ratios of known AGN-important galaxies are being measured in our ALMA program (Imanishi et al., in preparation), and they tend to show higher HCN-to- $\text{HCO}^+ J = 4-3$  flux ratios than NGC 1614, the template starburst galaxy (see also Imanishi et al. 2010a; Sakamoto et al. 2010; Iono et al. 2013). Since the  $J = 4-3$  lines of HCN and  $\text{HCO}^+$  are at higher frequencies (shorter wavelengths) than the lower  $J$  transition lines, the empirical energy diagnostic method, if established at  $J = 4-3$ , is applicable to more distant merging LIRGs using ALMA. This advantage is strengthened if HCN excitation is generally thermal up to the  $J = 4-3$  transition in AGN-important galaxies because HCN flux increases proportional to the square of frequency, partly compensating for the increase in Earth's atmospheric background emission at higher-frequency ALMA bands. However, if the excitation at HCN  $J = 4-3$  is sub-thermal, then HCN  $J = 3-2$  or  $J = 2-1$  lines may be better tracers of AGN in terms of actually obtainable S/N ratios with ALMA. Additional molecular line transition data at  $J = 3-2$  and  $2-1$  for starburst-dominated galaxies and AGN-important galaxies are needed (1) to distinguish whether high HCN-to- $\text{HCO}^+$  flux ratios at  $J = 4-3$  in AGN-important galaxies are due to HCN abundance enhancement and/or more HCN  $J = 4-3$  excitation than starbursts and (2) to identify the  $J$  transition lines that are practically the best diagnostic for separating AGNs from starburst-dominated galaxies.

## 5. SUMMARY

We performed HCN,  $\text{HCO}^+$ , and HNC  $J = 4-3$  line observations of the well-studied starburst galaxy NGC 1614 to trace the properties of the high-density molecular gas. Our results are summarized as follows:

1. HCN,  $\text{HCO}^+$ , and HNC  $J = 4-3$  emission are clearly detected in the nuclear regions of NGC 1614, but CS  $J = 7-6$  emission and HCN  $J=4-3$  line at a vibrationally-excited level ( $v_2=1$ ,  $l=1f$ ) are not.
2. HCN,  $\text{HCO}^+$ , and HNC  $J = 4-3$  emission at the northern and southern parts of the nucleus are red-

shifted and blueshifted, respectively, with respect to the nuclear velocity of this galaxy. When the emission is separated into the red and blue components, the red and blue components are strongest at  $0.6''$  north and south of the nucleus for all of the HCN,  $\text{HCO}^+$ , and HNC  $J = 4-3$  lines.

3. At the peak location of the red and blue components of these dense molecular gas tracers, the presence of active dusty starbursts is suggested, based on the infrared  $3.3 \mu\text{m}$  PAH emission, infrared  $8.7 \mu\text{m}$  dust continuum emission, and radio  $8.4 \text{ GHz}$  free-free emission, supporting the scenario that starbursts occur in dense molecular gas.
4. The dynamical mass derived from the red and blue dense molecular gas components, assuming rotational motion, is  $1.5\text{--}2.5 \times 10^9 M_\odot$  within  $\sim 2''$  in radius. This is similar to estimates previously obtained using other methods.
5. The HCN-to- $\text{HCO}^+$  flux ratios are smaller than unity, and the HCN-to-HNC flux ratios are higher than unity for  $J = 4-3$  in NGC 1614, which is a similar trend to previous observations of  $J = 1-0$  for starburst-dominated galaxies.

We thank E. Mullar and H. Nagai for their useful advice on ALMA data analysis. M.I. is supported by Grants-in-Aid for Scientific Research (no. 22012006). This paper makes use of the following ALMA data: ADS/JAO.ALMA#2011.0.00020.S. ALMA is a partnership of ESO (representing its member states), NSF (USA), and NINS (Japan), together with NRC (Canada) and NSC and ASIAA (Taiwan), in cooperation with the Republic of Chile. The Joint ALMA Observatory is operated by ESO, AUI/NRAO, and NAOJ.

## REFERENCES

- Aalto, S., Radford, S. J., E., Scoville, N. Z., & Sargent, A. I. 1997, *ApJ*, 475, L107
- Aalto, S., Wilner, D., Spaans, M., Wiedner, M. C., Sakamoto, K., Black, J. H., & Caldas, M. 2009, *A&A*, 493, 481
- Alonso-Herrero, A., Engelbracht, C. W., Rieke, M. J., Rieke, G. H., & Quillen, A. C. 2001, *ApJ*, 546, 952
- Bernard-Salas, J., et al. 2009, *ApJS*, 184, 230
- Brandl, B. R., et al. 2006, *ApJ*, 653, 1129
- Bryant, P., & Scoville, N. Z. 1999, *AJ*, 117, 2632
- Casoli, F., Willaime, M. -C., Viallefond, F., & Gerin, M. 1999, *A&A*, 346, 663
- Costagliola, F., et al. 2011, *A&A*, 528, 30
- De Robertis, M. M., & Shaw, R. A. 1988, *ApJ*, 329, 629
- Diaz-Santos, T., Alonso-Herrero, A., Colina, L., Packham, C., Radoski, J. T., & Telesco, C. M. 2008, *ApJ*, 685, 211
- Di Matteo, T., Springel, V., & Hernquist, L. 2005, *Nature*, 433, 605
- Downes, D., & Eckart, A. 2007, *A&A*, 468, L57
- Downes, D., & Solomon, P. M. 1998, *ApJ*, 507, 615
- Evans, A. S., Mazzarella, J. M., Surace, J. A., & Sanders, D. B. 2002, *ApJ*, 580, 749
- Gao, Y., & Solomon, P. M. 2004, *ApJS*, 152, 63
- Haan, S., et al. 2011, *AJ*, 141, 100
- Harada, N., Herbst, E., & Wakelam, V. 2010, *ApJ*, 721, 1570
- Hopkins, P. F., Hernquist, L., Cox, T. J., Di Matteo, T., Martini, P., Robertson, B., & Springel, V. 2005, *ApJ*, 630, 705
- Hopkins, P. F., Hernquist, L., Cox, T. J., Di Matteo, T., Robertson, B., & Springel, V. 2006, *ApJS*, 163, 1
- Imanishi, M., & Dudley, C. C. 2000, *ApJ*, 545, 701
- Imanishi, M., Dudley, C. C., & Maloney, P. R. 2006a, *ApJ*, 637, 114
- Imanishi, M., Imase, K., Oi, N., & Ichikawa, K. 2011, *AJ*, 141, 156
- Imanishi, M., Nakagawa, T., Ohyama, Y., Shirahata, M., Wada, T., Onaka, T., & Oi, N. 2008, *PASJ*, 60, S489
- Imanishi, M., & Nakanishi, K. 2006, *PASJ*, 58, 813
- Imanishi, M., Nakanishi, K., Kuno, N., & Kohno, K. 2004, *AJ*, 128, 2037
- Imanishi, M., Nakanishi, K., & Kohno, K. 2006b, *AJ*, 131, 2888
- Imanishi, M., Nakanishi, K., Tamura, Y., Oi, N., & Kohno, K. 2007, *AJ*, 134, 2366
- Imanishi, M., Nakanishi, K., Tamura, Y., & Peng, C. -H. 2009, *AJ*, 137, 3581
- Imanishi, M., Nakanishi, K., Yamada, M., Tamura, Y., & Kohno, K. 2010a, *PASJ*, 62, 201
- Imanishi, M., Nakagawa, T., Shirahata, M., Ohyama, Y., & Onaka, T. 2010b, *ApJ*, 721, 1233
- Iono, D., et al. 2007, *ApJ*, 659, 283
- Iono, D., et al. 2013, *PASJ*, in press (arXiv:1305.4535)
- Iono, D., Ho, P. T. P., Yun, M. S., Matsushita, S., Peck, A. B., & Sakamoto, K. 2004, *ApJ*, 616, L63
- Izumi, T., et al. 2013, *PASJ*, in press (arXiv:1306.0507)
- Kewley, L. J., Heisler, C. A., Dopita, M. A., & Lumsden, S. 2001, *ApJS*, 132, 37
- Knudsen, K. K., Walter, F., Weiss, A., Bolatto, A., Riechers, D. A., & Menten, K. 2007, *ApJ*, 666, 156
- Kohno, K. 2005, in *AIP Conf. Ser.* 783, *The Evolution of Starbursts*, ed. S. Hüttemeister, E. Manthey, D. Bomans, & K. Weis (New York: AIP), 203 (astro-ph/0508420)
- Komatsu, E., et al. 2009, *ApJS*, 180, 330
- König, S., Aalto, S., Müller, S., Beswick, R. J., & Gallagher III, J. S. 2013, *A&A*, 553, A72
- Krips, M., Neri, R., García-Burillo, S., Martín, S., Combes, F., Gracia-Carpio, J., & Eckart, A. 2008, *ApJ*, 677, 262
- Lintott, C., & Viti, S. 2006, *ApJ*, 646, L37
- Meijerink, R., & Spaans, M. 2005, *A&A*, 436, 397
- Meijerink, R., Spaans, M., & Israel, F. P. 2007, *A&A*, 461, 793
- Miles, J. W., Houck, J. R., Hayward, T. L., & Ashby, M. L. N. 1996, *ApJ*, 465, 191
- Moorwood, A. F. M. 1986, *A&A*, 166, 4
- Nakanishi, K., Okumura, S. K., Kohno, K., Kawabe, R., & Nakagawa, T. 2005, *PASJ*, 57, 575
- Neff, S. G., Hutchings, J. B., Stanford, S. A., & Unger, S. W. 1990, *AJ*, 99, 1088
- Olsson, E., Aalto, S., Thomasson, M., & Beswick, R. 2010, *A&A*, 513, A11
- Perez-Beaupuits, J. P., Aalto, S., & Gerebro, H. 2007, *A&A*, 476, 177
- Ridgway, S. E., Wynn-Williams, C. G., & Becklin, E. E. 1994, *ApJ*, 428, 609
- Rothberg, B., & Joseph, R. D. 2004, *AJ*, 128, 2098
- Sakamoto, K., et al. 2009, *ApJ*, 700, L104
- Sakamoto, K., Aalto, S., Costagliola, F., Martín, S., Ohyama, Y., Wiedner, M. C., & Wilner, D. J. 2013, *ApJ*, 764, 42
- Sakamoto, K., Aalto, S., Evans, A. S., Wiedner, M., & Wilner, D. 2010, *ApJ*, 725, L228
- Sanders, D. B., Mazzarella, J. M., Kim, D. -C., Surace, J. A., & Soifer, B. T. 2003, *ApJ*, 126, 1607
- Sanders, D. B., & Mirabel, I. F. 1996, *ARA&A*, 34, 749
- Scoville, N. Z., Sanders, D. B., Sargent, A. I., Soifer, B. T., & Tinney, C. G. 1989, *ApJ*, 345, L25
- Sellgren, K. 1981, *ApJ*, 245, 138
- Shier, L. M., Rieke, M. J., & Rieke, G. H. 1994, *ApJ* 433, L9
- Soifer, B. T. et al. 2001, *AJ*, 122, 1213
- Solomon, P. M., Downes, D., & Radford, S. J. E. 1992, *ApJ*, 387, L55
- Solomon, P. M., & Vanden Bout, P. A. 2005, *ARA&A*, 43, 677
- Springel, V., Di Matteo, T., & Hernquist, L. 2005, *MNRAS*, 361, 776
- Trung, D. V., Lo, K. Y., Kim, D. -C., Gao, Y., & Gruendl, R. A. 2001, *ApJ*, 556, 141
- Vaisanen, P., Rajpaul, V., Zijlstra, A. A., Reunanen, J., & Kotilainen, J. 2012, *MNRAS*, 420, 2209
- Veilleux, S., Kim, D. -C., Sanders, D. B., Mazzarella, J. M., & Soifer, B. T. 1995, *ApJS*, 98, 171
- Wilson, C. D., et al. 2008, *ApJS*, 178, 189
- Yuan, T. -T., Kewley, L. J., & Sanders, D. B. 2010, *ApJ*, 709, 884

TABLE 1  
THE *IRAS*-BASED INFRARED EMISSION PROPERTIES OF NGC 1614

Object	Redshift	$f_{12}$ [Jy]	$f_{25}$ [Jy]	$f_{60}$ [Jy]	$f_{100}$ [Jy]	$\log L_{\text{IR}}$ [ $L_{\odot}$ ]
(1)	(2)	(3)	(4)	(5)	(6)	(7)
NGC 1614 (IRAS 04315–0840)	0.016	1.38	7.50	32.12	34.32	11.6

NOTE. — Col.(1): Object name. Col.(2): Redshift. Col.(3)–(6):  $f_{12}$ ,  $f_{25}$ ,  $f_{60}$ , and  $f_{100}$  are *IRAS* fluxes at 12  $\mu\text{m}$ , 25  $\mu\text{m}$ , 60  $\mu\text{m}$ , and 100  $\mu\text{m}$ , respectively, taken from Sanders et al. (2003). Col.(7): Decimal logarithm of infrared (8–1000  $\mu\text{m}$ ) luminosity in units of solar luminosity ( $L_{\odot}$ ), calculated with  $L_{\text{IR}} = 2.1 \times 10^{39} \times D(\text{Mpc})^2 \times (13.48 \times f_{12} + 5.16 \times f_{25} + 2.58 \times f_{60} + f_{100})$  [ergs s $^{-1}$ ] (Sanders & Mirabel 1996).

TABLE 2  
LOG OF ALMA CYCLE 0 OBSERVATIONS OF NGC 1614

Line	Date [UT]	Antenna Number	Bandpass	Calibrator Flux	Phase
(1)	(2)	(3)	(4)	(5)	(6)
HCN/HCO $^{+}$ J=4–3	2011 November 15	16	3C454.3	Callisto	J0423–013
HNC J=4–3	2011 November 15	16	3C454.3	Callisto	J0423–013

NOTE. — Col.(1): Observed molecular line. Col.(2): Observing date in UT. Col.(3): Number of antennas used for observations. Cols.(4), (5), and (6): Band-pass, flux, and phase calibrators used for our NGC 1614 observations, respectively.

TABLE 3  
CONTINUUM EMISSION OF NGC 1614

Continuum	Frequency [GHz]	Flux [mJy beam $^{-1}$ ]	Peak Coordinate (RA,DEC)	rms [mJy beam $^{-1}$ ]	Synthesized Beam [arcsec $\times$ arcsec] ( $^{\circ}$ )
(1)	(2)	(3)	(4)	(5)	(6)
a	344	14.6 (45 $\sigma$ ) <sup>a</sup>	(04 34 00.01, –08 34 44.9)	0.32	1.5 $\times$ 1.3 (81 $^{\circ}$ )
b	351	10.9 (29 $\sigma$ ) <sup>a</sup>	(04 34 00.03, –08 34 44.9)	0.37	1.3 $\times$ 1.3 (–53 $^{\circ}$ )

NOTE. — Col.(1): Continuum "a" and "b" data were taken during observations of HCN/HCO $^{+}$  J = 4–3 and HNC J = 4–3, respectively. Col.(2): Central frequency of the continuum in [GHz]. Col.(3): Peak signal value in the continuum map in [mJy beam $^{-1}$ ], and detection significance, relative to the rms noise, in parentheses. Col.(4): The coordinate of the continuum emission peak in J2000. Col.(5): The rms noise ( $1\sigma$ ) of the continuum map in [mJy beam $^{-1}$ ]. Col.(6): The synthesized beam of the continuum map. Position angle is 0 $^{\circ}$  along the north-south direction, and increases in the counter-clockwise direction.

<sup>a</sup>We do not include possible systematic uncertainty, which is difficult to quantify.

TABLE 4  
MOLECULAR LINE FLUX IN NGC 1614

Line	Velocity component	Integrated intensity (moment 0) map			Beam [arcsec $\times$ arcsec] ( $^{\circ}$ )
		Peak [Jy beam $^{-1}$ km s $^{-1}$ ] (3)	rms [Jy beam $^{-1}$ km s $^{-1}$ ] (4)		
(1)	(2)				(5)
HCN J=4–3	all	1.7 (12 $\sigma$ )	0.14		1.5 $\times$ 1.3 (76 $^{\circ}$ )
	red	1.3 (14 $\sigma$ )	0.088		1.5 $\times$ 1.3 (76 $^{\circ}$ )
	blue	0.99 (9.4 $\sigma$ )	0.11		1.5 $\times$ 1.3 (76 $^{\circ}$ )
HCO $^{+}$ J=4–3	all	7.1 (33 $\sigma$ )	0.22		1.5 $\times$ 1.3 (76 $^{\circ}$ )
	red	5.2 (42 $\sigma$ )	0.12		1.5 $\times$ 1.3 (76 $^{\circ}$ )
	blue	5.7 (36 $\sigma$ )	0.16		1.5 $\times$ 1.3 (76 $^{\circ}$ )
HNC J=4–3	all	1.1 (7.0 $\sigma$ ) <sup>a</sup>	0.16		1.3 $\times$ 1.3 (–53 $^{\circ}$ )
	red	0.57 (6.9 $\sigma$ )	0.084		1.3 $\times$ 1.3 (–53 $^{\circ}$ )
	blue	1.1 (8.2 $\sigma$ )	0.13		1.3 $\times$ 1.3 (–54 $^{\circ}$ )
CS J=7–6	all	<0.45(<3 $\sigma$ ) <sup>b</sup>	0.15		1.5 $\times$ 1.4 (81 $^{\circ}$ )

NOTE. — Col.(1): Molecular line. Col.(2): Velocity component. The notations “all”, “red”, and “blue” mean all velocity components with significant signal detection, red component with  $v_{\text{opt}} \equiv c(\lambda - \lambda_0)/\lambda_0 > 4800$  km s $^{-1}$ , and blue component with  $v_{\text{opt}} < 4800$  km s $^{-1}$ , respectively. Col.(3): Peak flux in the integrated intensity (moment 0) map in [Jy beam $^{-1}$  km s $^{-1}$ ] and detection significance relative to the rms noise, in parentheses. Col.(4): The rms noise level (1 $\sigma$ ) in the moment 0 map in [Jy beam $^{-1}$  km s $^{-1}$ ]. Col.(5): Synthesized beam of the moment 0 map. Position angle is 0 $^{\circ}$  along the north-south direction and increases in the counter-clockwise direction.

<sup>a</sup>The peak position of the HNC J = 4–3 emission, integrating over all velocity components with significant signal detection, is two pixels (0.6 $''$ ) south of the continuum “b” peak, which could be explained by the stronger blue HNC emission component compared with the red component (Figure 5). See text in §3.

<sup>b</sup>The HCN J=4–3 to CS J=7–6 flux ratio is >3.7. This lower limit is lower than the ratios found in AGNs, and is comparable to those observed in starburst galaxies (Izumi et al. 2013).

TABLE 5  
GAUSSIAN FIT PARAMETERS TO MOLECULAR LINE EMISSION FROM NGC 1614

Line	Position	Gaussian line fit			
		Center [km s $^{-1}$ ] (3)	Peak [mJy] (4)	FWHM [km s $^{-1}$ ] (5)	Flux [Jy km s $^{-1}$ ] (6)
HCN J=4–3	all	4733 $\pm$ 25 + 4857 $\pm$ 14	11 $\pm$ 2 + 12 $\pm$ 4	171 $\pm$ 52 + 73 $\pm$ 30	2.8 $\pm$ 0.8
	peak	4822 $\pm$ 10	11 $\pm$ 1	131 $\pm$ 24	1.6 $\pm$ 0.3
	red	4853 $\pm$ 2	18 $\pm$ 2	68 $\pm$ 7	1.3 $\pm$ 0.2
	blue	4720 $\pm$ 17	6.2 $\pm$ 0.9	214 $\pm$ 42	1.4 $\pm$ 0.3
HCO $^{+}$ J=4–3	all	4718 $\pm$ 9 + 4858 $\pm$ 3	50 $\pm$ 3 + 70 $\pm$ 6	200 $\pm$ 20 + 72 $\pm$ 8	16.0 $\pm$ 1.4 <sup>a</sup>
		4650 $\pm$ 4 + 4755 $\pm$ 5 + 4857 $\pm$ 2	51 $\pm$ 6 + 49 $\pm$ 2 + 81 $\pm$ 8	70 $\pm$ 8 + 105 $\pm$ 31 + 72 $\pm$ 5	15.6 $\pm$ 1.9 <sup>a</sup>
	peak	4803 $\pm$ 4	41 $\pm$ 2	167 $\pm$ 9	7.3 $\pm$ 0.5
	red	4854 $\pm$ 1	72 $\pm$ 3	76 $\pm$ 2	5.8 $\pm$ 0.3
HNC J=4–3	blue	4715 $\pm$ 4	37 $\pm$ 2	180 $\pm$ 9	7.0 $\pm$ 0.5
	all	4718 $\pm$ 11 + 4859 $\pm$ 16	10 $\pm$ 2 + 7.8 $\pm$ 2.7	125 $\pm$ 27 + 50 $\pm$ 45	1.7 $\pm$ 0.5
	peak	4800 (fix)	3.6 $\pm$ 1.0	183 $\pm$ 75	0.7 $\pm$ 0.3
	red	4856 $\pm$ 3	13 $\pm$ 2	42 $\pm$ 7	0.6 $\pm$ 0.1
	blue	4714 $\pm$ 9	9.1 $\pm$ 1.4	116 $\pm$ 23	1.1 $\pm$ 0.3

NOTE. — Col.(1): Molecular line. Col.(2): Position and area for spectral extraction. “all” means spectra integrated over all regions of significant signal detection ( $\sim 3'' \times 3''$ ). The terms “peak”, “red”, and “blue” denote spectra within the beam size at the peak position of the continuum, red, and blue molecular line components, respectively. The coordinates of the red and blue peaks are (04 34 00.01, –08 34 44.3) and (04 34 00.01, –08 34 45.5) in J2000, respectively, for all of the HCN, HCO $^{+}$ , and HNC. For the “peak”, the continuum “a” peak coordinate (Table 3) is used for HCN and HCO $^{+}$ , and the continuum “b” peak (Table 3) is used for HNC. Cols. (3)–(6): Gaussian fits of the detected molecular emission lines. For “all”, double Gaussian fits are applied because emission lines are double peaked. For “all” of HCO $^{+}$ , a triple Gaussian fit is also applied for comparison. Col.(3): Central velocity of the Gaussian fits in [km s $^{-1}$ ]. Col.(4): Peak flux of the Gaussian fits in [mJy]. Col.(5): Full width at half maximum (FWHM) of the Gaussian fits in [km s $^{-1}$ ]. Col.(6): Total line flux, based on the Gaussian fits, in [Jy km s $^{-1}$ ].

<sup>a</sup>Wilson et al. (2008) derived the flux to be  $>14 \pm 3$  [Jy km s $^{-1}$ ] based on the Submillimeter Array (SMA) data, which probe emission over the spatial extent of  $<7''$ .



TABLE 6  
MOLECULAR LINE LUMINOSITY FOR NGC 1614

Line (1)	$[L_{\odot}]$ (2)	$[K \text{ km s}^{-1} \text{ pc}^2]$ (3)
HCN J=4-3	$(4.8 \pm 1.4) \times 10^3$	$(3.4 \pm 1.0) \times 10^6$
HCO <sup>+</sup> J=4-3	$(2.7 \pm 0.2) \times 10^4$	$(1.9 \pm 0.2) \times 10^7$
HNC J=4-3	$(3.0 \pm 0.9) \times 10^3$	$(1.9 \pm 0.6) \times 10^6$

NOTE. — Col.(1): Molecular line. Col.(2): Luminosity in units of  $[L_{\odot}]$ . Col.(3): Luminosity in units of  $[K \text{ km s}^{-1} \text{ pc}^2]$ .

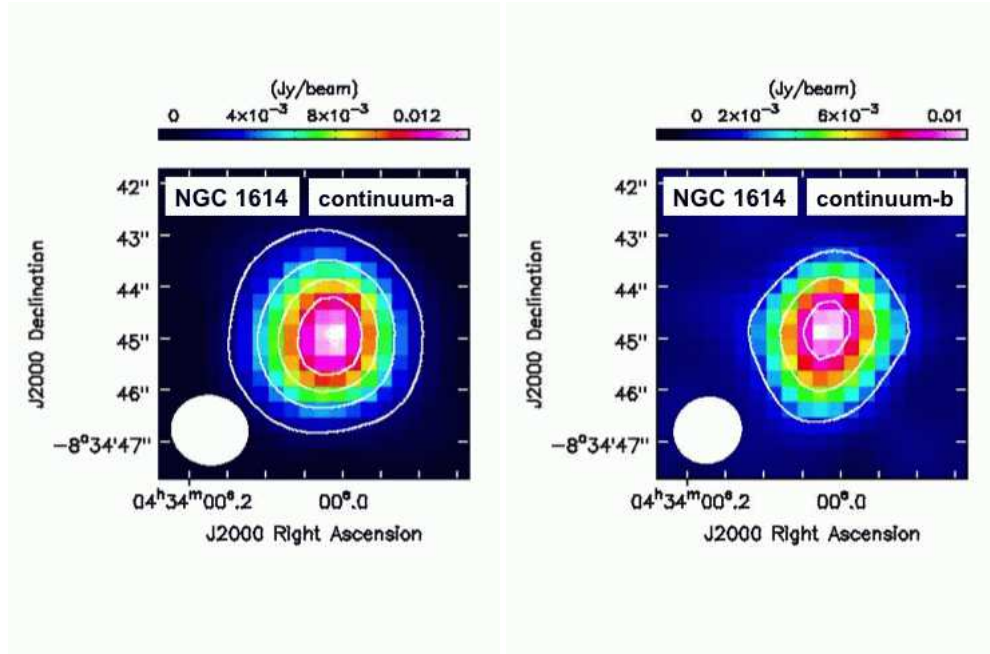
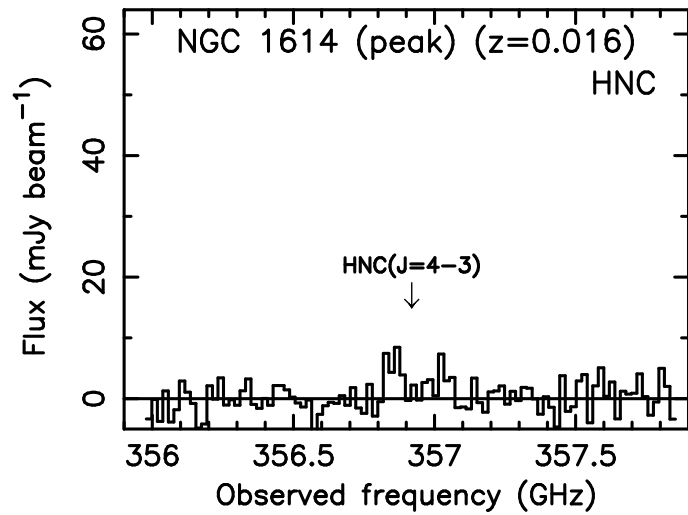
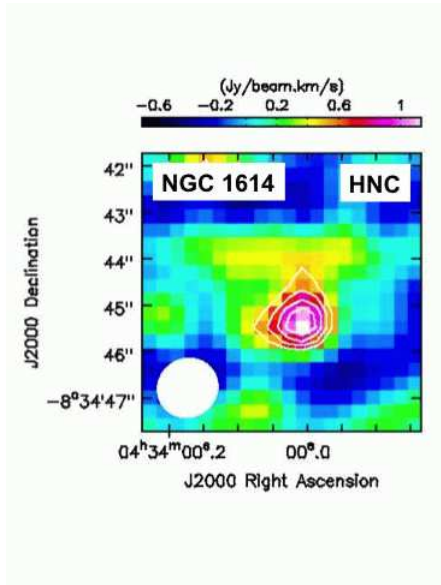
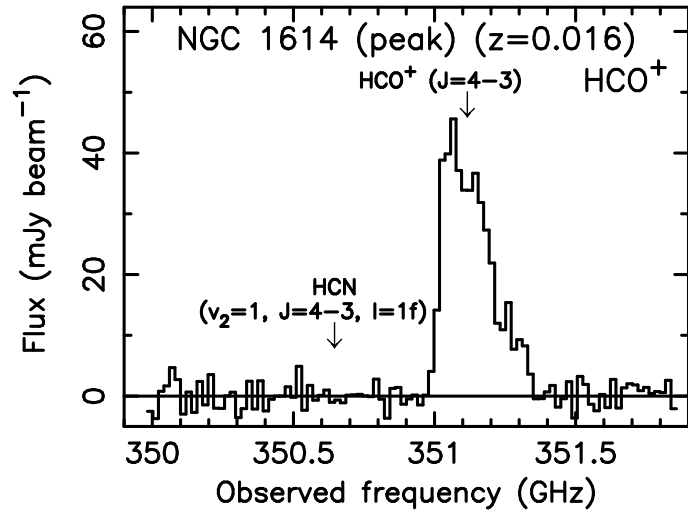
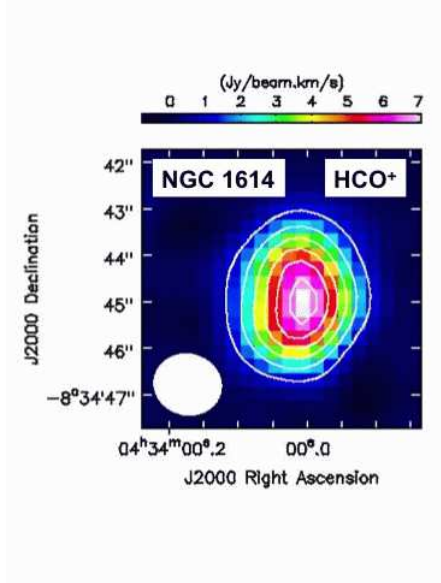
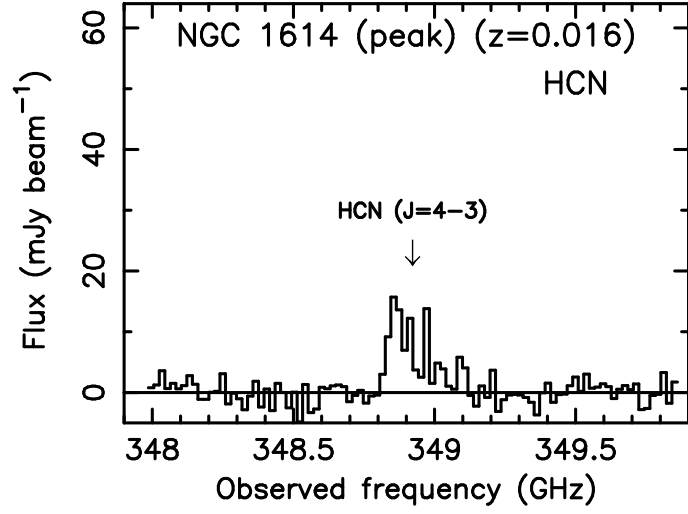
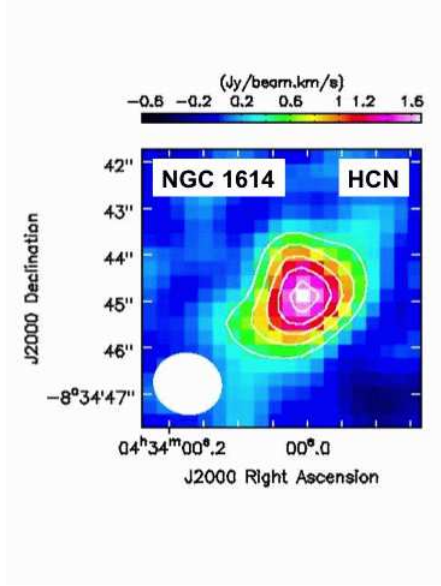


FIG. 1.— Continuum maps. North is top, and east is to the left. The continuum “a” (*Left*) and “b” (*Right*) data were taken during observations of the HCN/HCO<sup>+</sup> J = 4–3 and HNC J = 4–3 lines, respectively. Contours are 5σ, 15σ, 25σ, 35σ, 45σ for continuum “a” and 5σ, 15σ, 25σ for continuum “b”. The 1 σ level is shown in Table 3 and slightly differs between continua “a” and “b”. The continuum “a” data have higher detection significance than the continuum “b” data, and the peak position of the continuum “a” emission is (RA, DEC) = (04 34 00.01, −08 34 44.9) in J2000. We define this coordinate as the nucleus of NGC 1614 in this paper. The synthesized beams are shown as filled white circles at the bottom left of the individual figures.



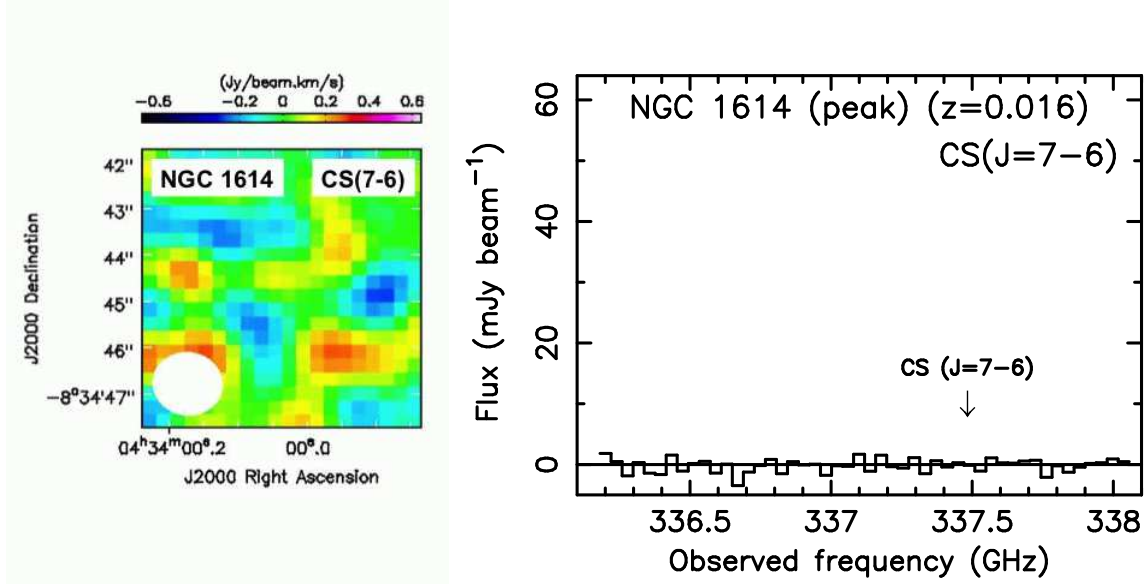


FIG. 2.— (*Left*): Integrated intensity (moment 0) maps of HCN  $J = 4-3$ ,  $\text{HCO}^+ J = 4-3$ , HNC  $J = 4-3$ , and CS  $J = 7-6$  lines of NGC 1614. North is top, and east is to the left. Signals in channels where line emission is recognizable are integrated to produce the moment 0 maps. Contours of the moment 0 maps are  $3\sigma$ ,  $5\sigma$ ,  $7\sigma$ ,  $9\sigma$ , and  $11\sigma$  for HCN,  $5\sigma$ ,  $10\sigma$ ,  $15\sigma$ ,  $20\sigma$ ,  $25\sigma$ , and  $30\sigma$  for  $\text{HCO}^+$ , and  $3\sigma$ ,  $4\sigma$ ,  $5\sigma$ , and  $6\sigma$  for HNC. For CS  $J = 7-6$ , no emission feature with  $\geq 3\sigma$  is seen. The  $1\sigma$  level is summarized in Table 4. (*Right*): The molecular line spectra within the beam size at the continuum peak position are shown. HCN  $J = 4-3$ ,  $\text{HCO}^+ J = 4-3$ , and CS  $J = 7-6$  line spectra are extracted at the continuum “a” peak position (Table 3), and HNC  $J = 4-3$  spectrum is extracted at the continuum “b” peak position (Table 3). The down arrows indicate the expected observed frequency of HCN  $J = 4-3$ ,  $\text{HCO}^+ J = 4-3$ , HNC  $J = 4-3$ , and CS  $J = 7-6$  lines at a redshift of  $z = 0.016$ . In the  $\text{HCO}^+ J = 4-3$  line spectrum, the observed frequency of the vibrationally excited HCN line ( $v_2 = 1$ ,  $J = 4-3$ ,  $l = 1f$ ;  $\nu_{\text{rest}} = 356.256$  GHz) (Sakamoto et al. 2010) is shown, but its detection is not clear. Assuming the same line profile as  $\text{HCO}^+ J = 4-3$ , the flux of HCN  $J = 4-3$  at  $v_2 = 1$  ( $l = 1f$ ) is estimated to be  $< 0.45$  [ $\text{Jy beam}^{-1} \text{ km s}^{-1}$ ] ( $< 3\sigma$ ), which is  $< 28\%$  of that of HCN  $J = 4-3$  at  $v = 0$ .

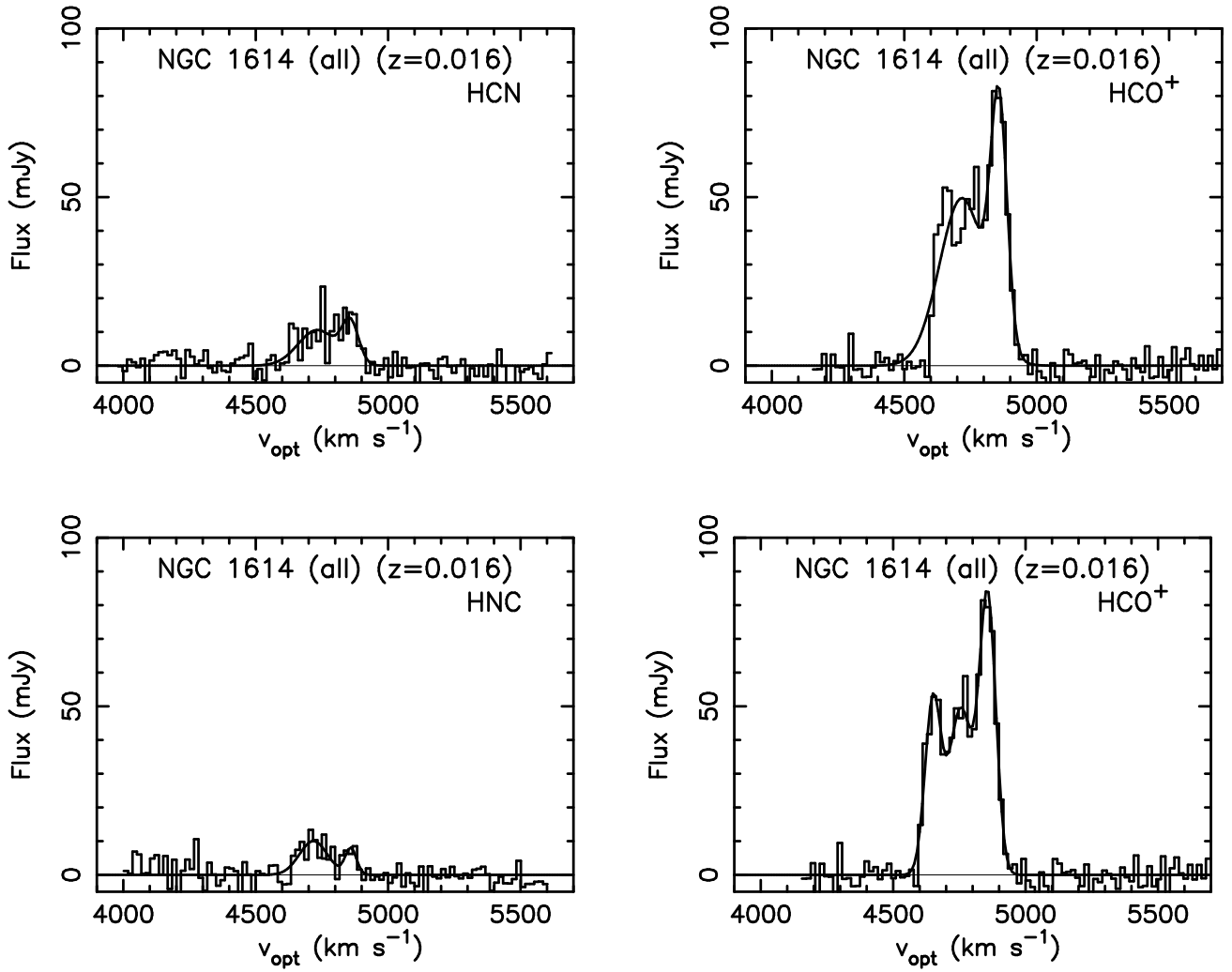


FIG. 3.— HCN, HCO<sup>+</sup>, and HNC J = 4–3 emission line spectra of NGC 1614 integrated over the region of significant signal detection ( $\sim 3'' \times 3''$ ). Gaussian fits (Table 5) are overplotted as the solid curved line. For the brightest HCO<sup>+</sup> J = 4–3 line, the triple Gaussian fit is also overplotted (lower-right panel).

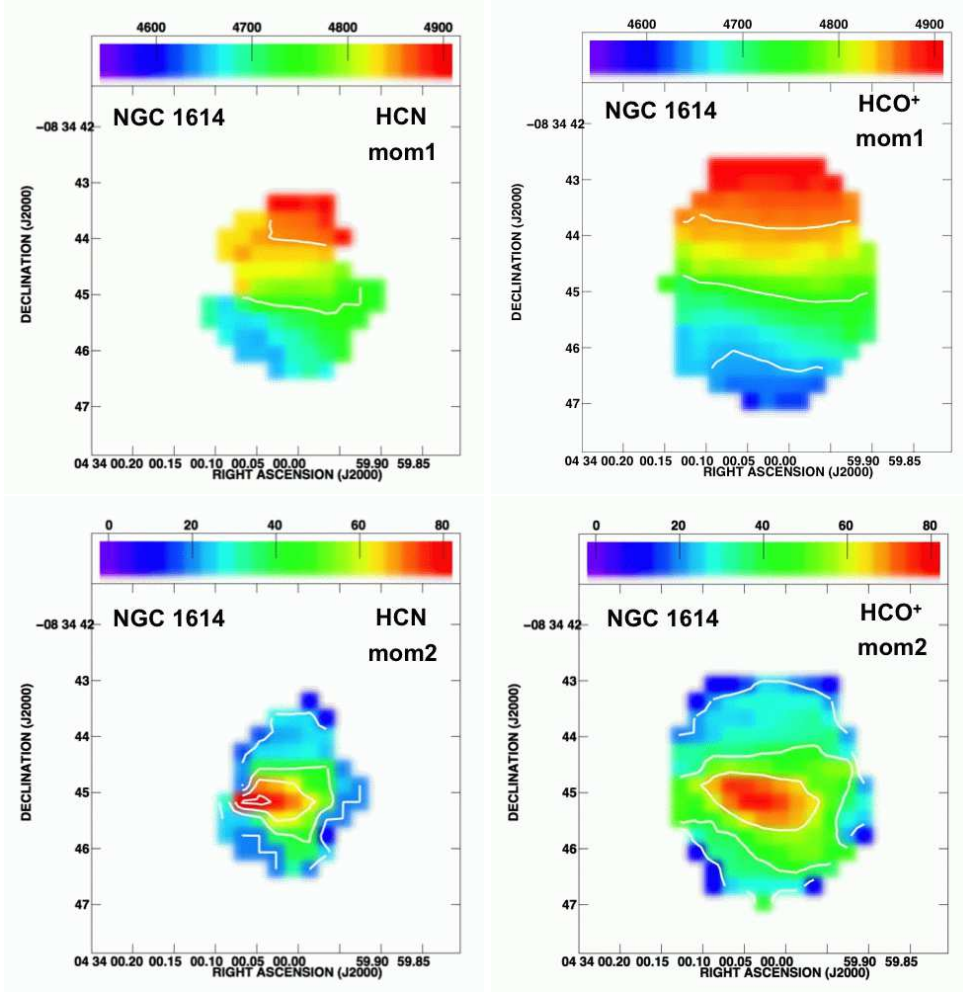


FIG. 4.— Intensity weighted mean velocity (moment 1) and intensity weighted velocity dispersion (moment 2) maps of HCN and HCO<sup>+</sup> J = 4–3 emission lines from NGC 1614. The velocity is in  $v_{\text{opt}} \equiv c (\lambda - \lambda_0) / \lambda_0$ . (*Upper Left*): Moment 1 map of HCN J = 4–3 emission. Contours are 4750 and 4850 [km s<sup>−1</sup>]. (*Upper Right*): Moment 1 map of HCO<sup>+</sup> J = 4–3 emission. Contours are 4650, 4750, and 4850 [km s<sup>−1</sup>]. (*Lower Left*): Moment 2 map of HCN J = 4–3 emission. Contours are 20, 40, 60, and 80 [km s<sup>−1</sup>]. (*Lower Right*): Moment 2 map of HCO<sup>+</sup> J = 4–3 emission. Contours are 20, 40, and 60 [km s<sup>−1</sup>].

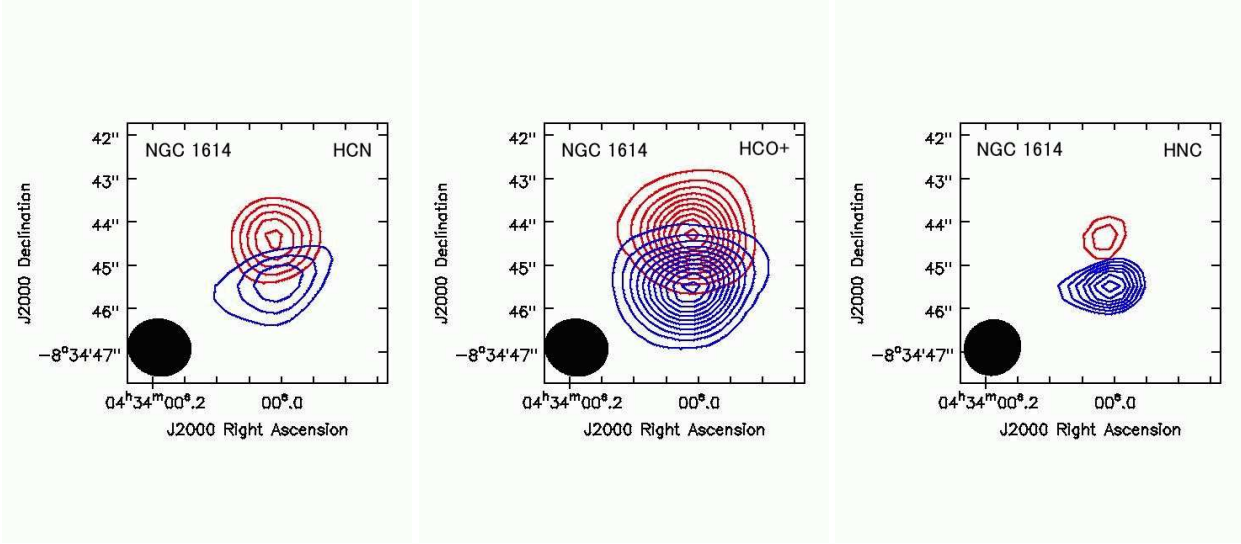


FIG. 5.— Contours of red and blue components of HCN,  $\text{HCO}^+$ , and HNC  $J = 4-3$  emission lines. By adopting a nuclear velocity for NGC 1614 ( $z = 0.016$ ) of  $v_{\text{opt}} = 4800 \text{ [km s}^{-1}\text{]}$ , emission with  $v_{\text{opt}} > 4800 \text{ [km s}^{-1}\text{]}$  and  $< 4800 \text{ [km s}^{-1}\text{]}$  is integrated for the red and blue components, respectively. The coordinates of the emission peaks of the red and blue components are  $(04\ 34\ 00.01, -08\ 34\ 44.3)$  and  $(04\ 34\ 00.01, -08\ 34\ 45.5)$  in J2000, respectively, for all the HCN,  $\text{HCO}^+$ , and HNC  $J = 4-3$  lines. For HCN, the contour starts at  $0.4 \text{ [Jy km s}^{-1}\text{]}$  and increases with  $0.2 \text{ [Jy km s}^{-1}\text{]}$ . For  $\text{HCO}^+$ , the contour starts at  $0.5 \text{ [Jy km s}^{-1}\text{]}$  and increases with  $0.5 \text{ [Jy km s}^{-1}\text{]}$ . For HNC, the contour starts at  $0.4 \text{ [Jy km s}^{-1}\text{]}$  and increases with  $0.1 \text{ [Jy km s}^{-1}\text{]}$ .

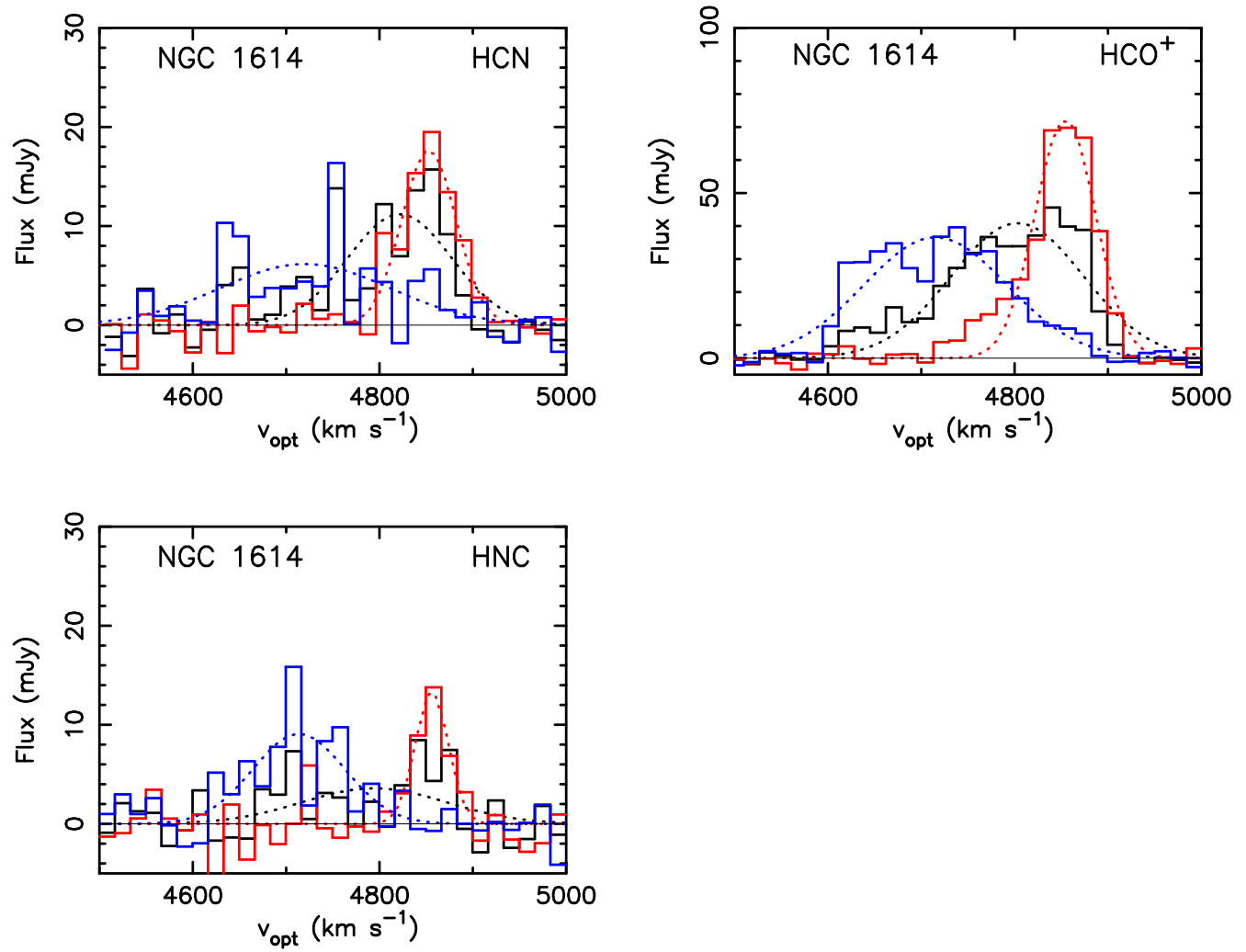


FIG. 6.— Spectra of NGC 1614. The black, red, and blue solid lines are spectra within the beam size at the nuclear position (04 34 00.01,  $-08^{\circ}34'44.9''$ ) in J2000, the peak position of the red component (04 34 00.01,  $-08^{\circ}34'44.3''$ ) in J2000, and the peak position of the blue component (04 34 00.01,  $-08^{\circ}34'45.5''$ ) in J2000. Gaussian fits are overplotted as dashed lines.



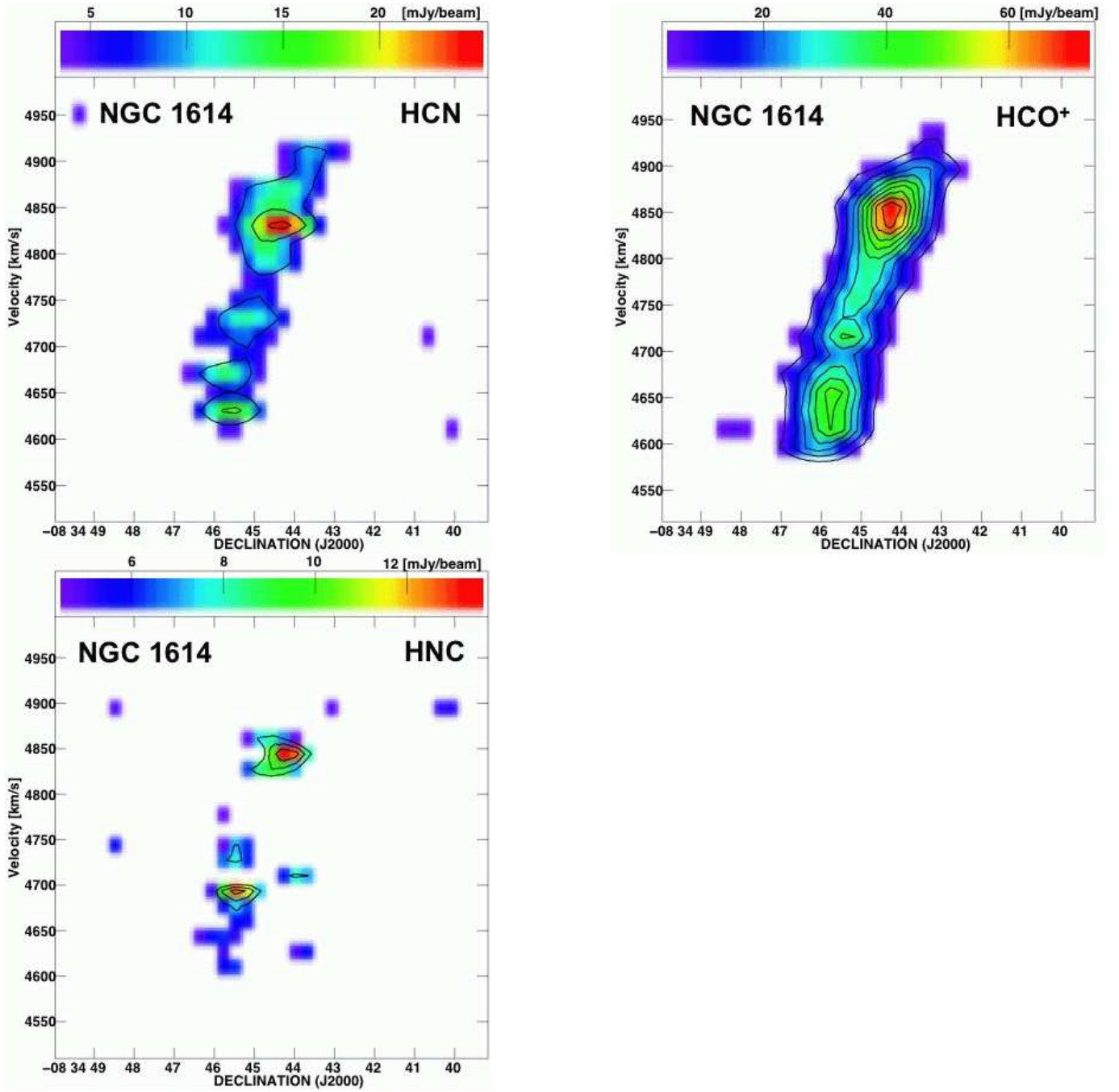


FIG. 7.— A position-velocity diagram along the north-south direction through the nucleus (continuum “a” peak). The abscissa is declination in J2000. North is to the right, and south is to the left. The ordinate is optical LSR velocity. The upper part of the y-axis is higher velocity, and the lower part is lower velocity. For HCN, the contour starts at  $7.6 \text{ [mJy beam}^{-1}]$  and increases with  $7.6 \text{ [mJy beam}^{-1}]$ . For HCO<sup>+</sup>, the contour starts at  $7.2 \text{ [mJy beam}^{-1}]$  and increases with  $7.2 \text{ [mJy beam}^{-1}]$ . For HNC, the contour starts at  $4.6 \text{ [mJy beam}^{-1}]$  and increases with  $2.3 \text{ [mJy beam}^{-1}]$ .

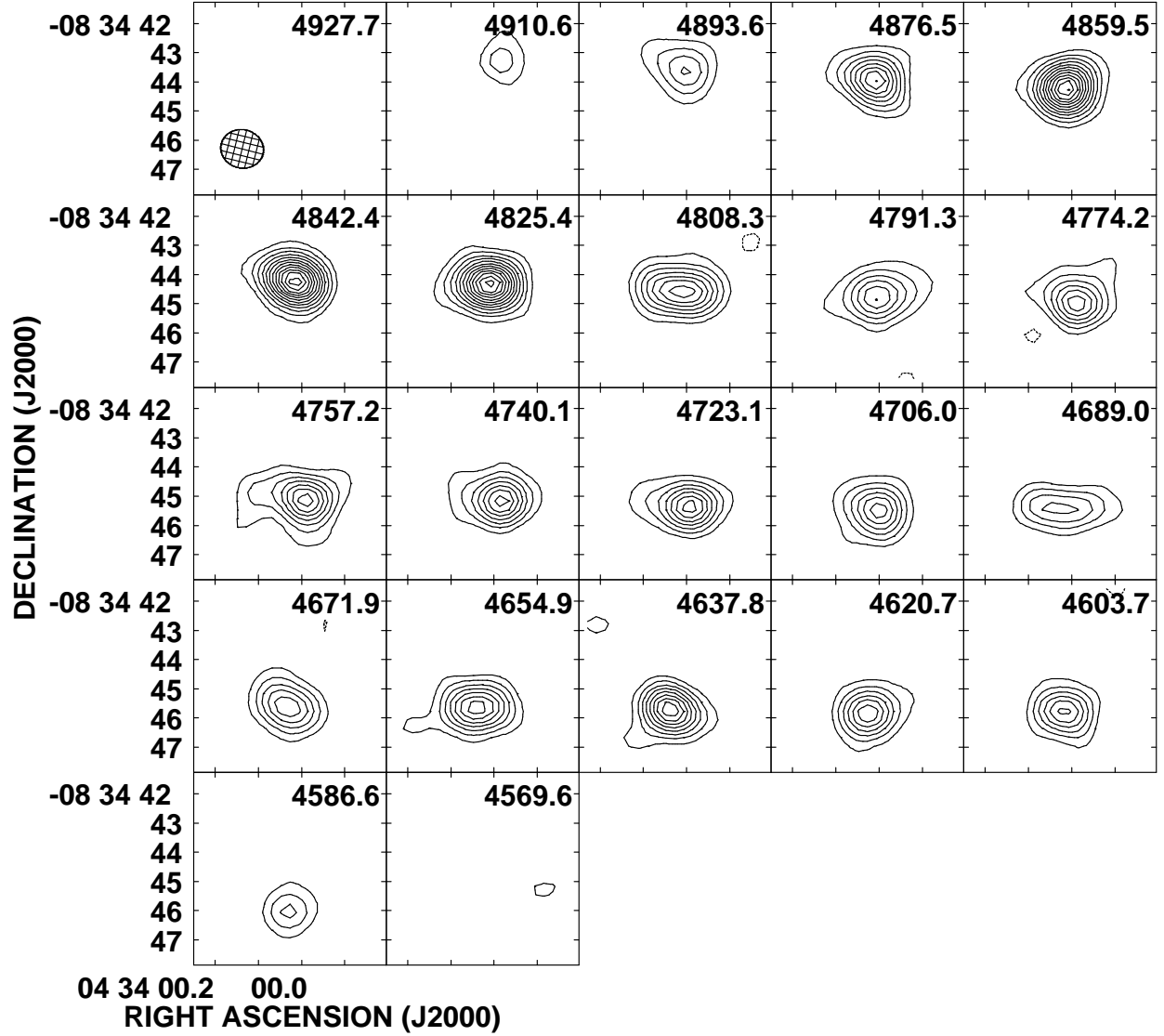


FIG. 8.— A channel map of  $\text{HCO}^+$   $J = 4-3$  emission in units of optical LSR velocity. Contours start at  $5.55 \text{ [mJy beam}^{-1}]$  and increase with  $5.55 \text{ [mJy beam}^{-1}]$ . The dashed contours are  $-5.55 \text{ [mJy beam}^{-1}]$ . The rms noise level of each channel is  $\sim 1.85 \text{ [mJy beam}^{-1}]$ . The number at the upper right part of each panel is velocity in  $[\text{km s}^{-1}]$ , and the synthesized beam pattern is shown at the lower left part of the top left panel.

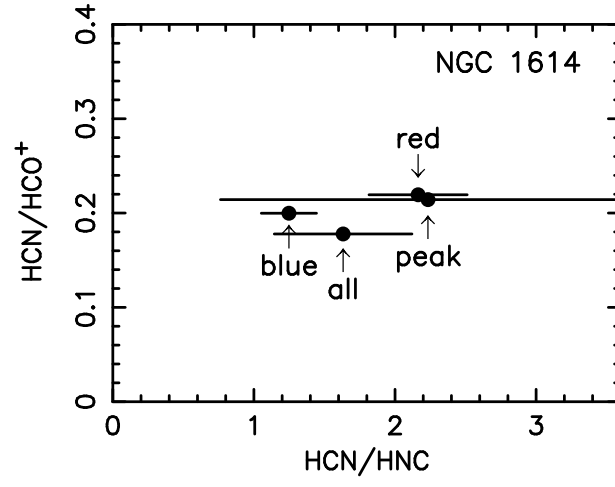


FIG. 9.— The HCN-to-HNC flux ratio (abscissa) and HCN-to-HCO<sup>+</sup> flux ratio (ordinate) at J = 4-3 transition. Data at “all”, “peak”, “red”, and “blue” positions in Table 5 are used.